

Article

Investigation of the Ionospheric Effects of the Solar Eclipse of April 8, 2024 Using Multi-Instrument Measurements

Aritra Sanyal ¹, Bhuvnesh Brawar ², Sovan Kumar Maity ^{1,3}, Shreyam Jana ¹, Jean Marie Polard ⁴, Peter Newton ⁵, George S. Williams ⁶, Stelios M. Potirakis ^{7,8,9}, Haris Haralambous ⁸, Georgios Balasis ^{9,*}, James Brundell ¹⁰, Pradipta Panchadhyayee ^{1,11}, Abhirup Datta ², Ajeet K. Maurya ¹², Saibal Ray ¹³ and Sudipta Sasmal ^{1,7,*}

- ¹ Institute of Astronomy Space and Earth Science, P 177, CIT Road, Scheme 7m, Kolkata 700054, India; aritra@iases.org.in (A.S.); sovan@iases.org.in (S.K.M.); shreyam@iases.org.in (S.J.); pradipta@iases.org.in (P.P.)
 - ² Department of Astronomy, Astrophysics and Space Engineering, Indian Institute of Technology Indore, Indore 453552, India; phd2101121005@iiti.ac.in (B.B.); abhirup.datta@iiti.ac.in (A.D.)
 - ³ Uttar Amtalia Gita Rani Vidyabhawan (H.S), Uttar Amtalia, Contai 721427, India
 - ⁴ Independent Researcher, 115 Napier Road, Glenrothes, Fife KY6 1DU, Scotland, UK; contact@polard.fr
 - ⁵ Independent Researcher, 1 lieudit Boutil, F-22540 Louargat, France; peter@iases.org.in
 - ⁶ Independent Researcher, 1119 Terrapin Swamp Rd, Wakefield, VA 23888-3103, USA; physicist@websterling.com
 - ⁷ Department of Electrical and Electronics Engineering, Ancient Olive Grove Campus, University of West Attica, 12244 Egaleo-Athens, Greece; spoti@uniwa.gr
 - ⁸ Department of Electrical Engineering, Computer Engineering and Informatics, School of Engineering, Frederick University, Nicosia 1036, Cyprus; eng.hh@frederick.ac.cy
 - ⁹ Institute for Astronomy, Astrophysics, Space Applications and Remote Sensing, National Observatory of Athens, Metaxa and Vasileos Pavlou, Penteli, 15236 Athens, Greece
 - ¹⁰ Department of Physics, University of Otago, P.O. Box 56, Dunedin 9016, New Zealand; james@brundell.co.nz
 - ¹¹ Department of Physics, Prabhat Kumar College, Karkuli, Contai 721404, India
 - ¹² Department of Physics, Babasaheb Bhimrao Ambedkar University, Vidya Vihar, Raebareli Road, Lucknow 226025, India; ajeet.phys@email.bbau.ac.in
 - ¹³ Centre for Cosmology, Astrophysics and Space Science (CCASS), GLA University, Mathura 281406, India; saibal@iases.org.in
- * Correspondence: gbalasis@noa.gr (G.B.); sudipta@iases.org.in (S.S.)



Academic Editor: Sandro Radicella

Received: 23 December 2024

Revised: 22 January 2025

Accepted: 27 January 2025

Published: 31 January 2025

Citation: Sanyal, A.; Brawar, B.; Maity, S.K.; Jana, S.; Polard, J.M.; Newton, P.; Williams, G.S.; Potirakis, S.M.; Haralambous, H.; Balasis, G.; et al. Investigation of the Ionospheric Effects of the Solar Eclipse of April 8, 2024 Using Multi-Instrument Measurements. *Atmosphere* **2025**, *16*, 161. <https://doi.org/10.3390/atmos16020161>

Copyright: © 2025 by the authors. Licensee MDPI, Basel, Switzerland. This article is an open access article distributed under the terms and conditions of the Creative Commons Attribution (CC BY) license (<https://creativecommons.org/licenses/by/4.0/>).

Abstract: Solar eclipses present a valuable opportunity for controlled in situ ionosphere studies. This work explores the response of the upper atmosphere's F-layer during the total eclipse of April 8, 2024, which was primarily visible across North and South America. Employing a multi-instrument approach, we analyze the impact on the ionosphere's Total Electron Content (TEC) and Very Low Frequency (VLF) signals over a three-day period encompassing the eclipse (April 7 to 9, 2024). Ground-based observations leverage data from ten International GNSS Service (IGS)/Global Positioning System (GPS) stations and four VLF stations situated along the eclipse path. We compute vertical TEC (*VTEC*) alongside temporal variations in the VLF signal amplitude and phase to elucidate the ionosphere's response. Notably, the IGS station data reveal a decrease in *VTEC* during the partial and total solar eclipse phases, signifying a reduction in ionization. While VLF data also exhibit a general decrease, they display more prominent fluctuations. Space-based observations incorporate data from Swarm and COSMIC-2 satellites as they traverse the eclipse path. Additionally, a spatiotemporal analysis utilizes data from the Global Ionospheric Map (GIM) database and the DLR's (The German Aerospace Center's) database. All space-based observations consistently demonstrate a significant depletion in *VTEC* during the eclipse. We further investigate the correlation between the percentage change in *VTEC* and the degree of solar obscuration, revealing a positive relationship. The consistent findings obtained from this comprehensive observational campaign bolster our understanding of the physical mechanisms governing ionospheric variability during solar eclipses. The observed depletion in *VTEC* aligns with the established principle that reduced solar radiation leads

to decreased ionization within the ionosphere. Finally, geomagnetic data analysis confirms that external disturbances do not significantly influence our observations.

Keywords: solar eclipse; vertical total electron content; VLF radio wave; multi-instrument observations; global ionospheric map

1. Introduction

A solar eclipse plays a crucial role in influencing the dynamics of the ionosphere, a region in the Earth's upper atmosphere extending approximately from 70 km to 1000 km in altitude. This layer, composed of ionized particles influenced by solar radiation, undergoes rapid changes during an eclipse. When the Moon aligns with the Sun, it temporarily obscures the solar disk, casting a shadow on Earth and causing a solar eclipse, which can be partial, total, or annular, depending on the alignment and relative distances of the Earth, Moon, and Sun. The reduction in solar radiation during an eclipse leads to abrupt changes in the ionosphere's electron density and temperature. These variations propagate through the ionosphere via ion-neutral coupling, affecting radio wave propagation, atmospheric dynamics, and geomagnetic conditions.

Moreover, the ionospheric response to a solar eclipse offers valuable insights into the underlying physical processes governing the Earth's upper atmosphere. By analyzing the spatiotemporal evolution of ionospheric parameters during eclipses, we can refine existing models of ionospheric dynamics, elucidate the effects of solar variability on terrestrial climate, and enhance the accuracy of space weather forecasting [1–6]. This paper delves into the multifaceted relationship between the ionosphere and solar eclipses, exploring the mechanisms driving ionospheric changes during these celestial events and their broader implications for atmospheric science, space weather research, and telecommunications technology. Through a comprehensive synthesis of observational data, we aim to deepen our understanding of the ionospheric response to solar eclipses and its significance for Earth's interconnected atmospheric system.

The ionosphere's electron content is a vital parameter for understanding its behavior. The Total Electron Content (TEC) is the measure of the total number of electrons along a column from a satellite to a receiver on Earth or on a satellite (such as Swarm). It is expressed in TEC Units (TECU), with 1 TECU corresponding to 10^{16} electrons/m². On the other hand, electron density in the ionosphere refers to the concentration of free electrons in a given volume. It is usually expressed in electrons per cubic meter (electrons/m³). The F2 layer, a key ionosphere region, is strongly linked to solar radiation. Its electron density rises after sunrise due to photoionization, peaking around noon or afternoon. As sunlight weakens after sunset, the F2 layer's electron density diminishes. The ionosphere affects radio waves passing through it. Free electrons cause the waves to deviate from their original path. This is particularly important for the Global Positioning System (GPS), a key Global Navigation Satellite System (GNSS) component. When GPS signals travel through the ionosphere, they experience a delay directly proportional to TEC. We can study the Earth's ionosphere by measuring TEC with dual-frequency GPS receivers. The UNAVCO Geodesy Advancing Geosciences and EarthScope (GAGE) Facility analyzes data from a network of over 2000 GPS receivers. These continuously operating stations, spread across North America, the Caribbean, and the high Arctic, track Earth's surface movement by recording position changes (time series) and velocities. Although the primary focus of GAGE is to study crustal motion, the data it collects can also be used to study TEC indirectly.

To analyze the impact of the solar eclipse on the ionosphere, we utilized data from the ESA's Swarm satellite mission. The swarm constellation consists of three satellites (Alpha, Bravo, and Charlie) launched in 2013 to study Earth's magnetic field. Our study focused on data from the Swarm-B satellite. Previous research documented the effects of solar eclipses on the ionosphere for decades [7–10]. This natural phenomenon offers a valuable opportunity to investigate how the Sun's radiation influences the ionosphere–thermosphere–mesosphere (ITM) system [11]. This study specifically examined variations in *VTEC* and electron density (*Ne*) during the total solar eclipse of 8 April 2024.

The Constellation Observing System for Meteorology, Ionosphere, and Climate-2/Formosa Satellite Mission 7 (COSMIC-2) GNSS Radio Occultation (RO) constellation, the successor to the successful COSMIC-1 program, consists of six identical micro-satellites. Each satellite carries a Tiny Ionospheric Photometer (TIP) and a Tri-Band-Beacon (TBB), which work together to enhance the accuracy and utility of ionospheric observations. These satellites orbit in six circular paths inclined at approximately 72° and at an altitude of about 800 km, providing various measurements, including GPS-based RO data, to probe the Earth's ionosphere and atmosphere. In this study, we observed the variation of the *Ne* profile due to the total solar eclipse.

To compare and validate regional TEC models, global Vertical Total Electron Content (*VTEC*) values are obtained from the Global Ionosphere Maps (GIMs) provided by the International GNSS Service (IGS) network. GIM is an effective tool for studying the ionospheric *VTEC* response during seismic activity and solar eclipses. GIM data are available at 2 h, 1 h, 30 min, and 15 min.

The German Aerospace Center's (DLR's) global TEC maps offer detailed Vertical Total Electron Content (*VTEC*) data for a shell-height of 400 km, significantly enhancing GNSS positioning accuracy compared to the Space Weather Application Center Ionosphere (SWACI) near real-time TEC map. Real-time GPS data from various sources by the German Federal Agency for Cartography and Geodesy in Frankfurt undergo preprocessing to derive calibrated slant TEC (*STEC*) values. These calibrated *STEC* values are then used to estimate coefficients for the Neustrelitz Total Electron Content Model (NTCM), which establishes the ionospheric background [12]. Integrating these measurements into the NTCM model allows for continuously updating a *VTEC* matrix every 5 min, with a spatial resolution of 2.5° latitude by 5° longitude. This matrix is stored in JSON format, ensuring users receive timely and accurate updates.

Radio waves emitted by VLF transmitters propagate within the waveguide formed by the lower ionosphere and the Earth's surface. Significant variations in the amplitude and phase of the received signals are attributed to changes in the lower ionosphere. Previous studies explored the analysis of the received VLF signals during eclipses, typically involving monitoring one to three transmitters (Tx) by one receiver (Rx). The first documented instance of an eclipse effect on VLF signals was reported by [13] on the GBR (Tx in Rugby, England) to Cambridge (Rx) path during a partial eclipse in 1949. A notable 35° change in phase was observed due to a 30% solar obscuration (Sun blockage). Studies focusing on short paths, defined as less than 1000 km, have been infrequent but indicate amplitude increases of 2 or 3 dB and phase decreases ranging from 60° to 100° [14]. For medium paths ranging from 1000 km to 10,000 km, [15] documented that signal propagation characteristics undergo significant changes, including an increase in amplitude and a phase shift. [16] presented findings from the total solar eclipse in Europe on 11 August 1999. Utilizing five receiving sets to monitor multiple stations, they analyzed 17 paths, varying in length from 90 km to 14,510 km. Their key observation was that for shorter propagation paths (<2000 km), the amplitude change was positive, indicating signal enhancement, while for paths exceeding 10,000 km, the amplitude change was negative. [17,18] examined the

effects of the solar eclipse on 22 July 2009, and 21 August 2017 on VLF signals across various propagation paths in the Indian subcontinent and USA respectively. Similar comprehensive analysis had been reported for multiple eclipses using ground- and space-based observations by [19–21]. [22] reported an exciting work using VLF remote sensing during the solar eclipse on 7 March 1970, where the depletion of the ionospheric reflection height was investigated through radio atmospherics (Tweeks). In this present study, signals of the medium path from four transmitters were utilized: NPM at 21.4 kHz in Lualualei, HA, USA; NAA at 24.0 kHz in Grimeton, Sweden; NLK at 24.8 kHz in Seattle, WA, USA; and NML at 25.2 kHz in LaMoure, ND, USA. Variations in the amplitude of the VLF signals recorded by a receiver located in rural SE Virginia, USA, were observed.

2. Materials and Methods

On 8 April 2024, a total solar eclipse occurred across North America, Canada, Mexico, and many countries in South and Central America. The partial eclipse began at 15:42 UTC and concluded at 20:52 UTC. The period of totality, during which the Moon completely obscured the Sun, was visible along a narrow path that stretched from Sinaloa to Coahuila in Mexico, from Texas to Maine in the United States, and from Ontario to Newfoundland in Canada. This totality phase started at 16:38 UTC and ended at 19:55 UTC.

In this manuscript, we investigated the ionospheric response to the total solar eclipse by analyzing four significant parameters: $VTEC$, Ne , and the phase and amplitude of VLF signals. For $VTEC$ computation, we employed four different methods: (a) Estimated $VTEC$ from IGS stations, (b) GIM database, (c) DLR ionospheric map database and (d) $VTEC$ data from Swarm satellites to GNSS altitude. Data were collected from six GNSS-IGS stations and four UNAVCO-IGS stations. Among the six GNSS-IGS stations, the total eclipse was observed from the IGS station NRC1, while the station INEG experienced a minimum obscuration of 90.67%. Among the four UNAVCO-IGS stations, the total eclipse was observed from station P777, with the station TNCU experiencing a minimum obscuration of 90.94%. Figure 1 illustrates the locations of the GNSS-IGS stations (marked with yellow diamonds) and the UNAVCO-IGS stations (marked with orange circles), as well as the totality belt (indicated by the red solid curve) spanning the North and South American landmasses. We also computed electron density (Ne) profile as a numerical integration of radio occupation up to the Cosmic satellite altitude.

The Receiver Independent Exchange Format (RINEX) observation and navigation files used for the computation of $VTEC$ are sourced from the IGS data archive <https://cddis.nasa.gov/archive>, (accessed on 15 April 2024). $STEC$ corresponds to measure the number of free electrons (expressed in TECU) along a slant path between a satellite and a receiving station. A useful software was developed by Gopi Seemala for all sorts of computations on $VTEC$, $STEC$, satellite and receiver corrections, and bias, and made accessible on the website (<http://seemala.blogspot.com>, accessed on 15 April 2024). The program code and its use for $VTEC$ computation are mentioned in some important works [23, 24]. We attempted to convert the $STEC$ into an equivalent $VTEC$ by using the thin shell approximation and using the technique given by [26–31].

The geometrical configuration of the Sun and the Moon during the eclipse, as suggested by [32], is shown in Figure 2a. In Figure 2b–d, we present the luminance and shadow spatiotemporal graph across the totality belt on the map. The luminance is calculated at the eclipse's beginning, maximum, and end. Figure 2b shows the luminance at the start of the total solar eclipse on the totality belt. Similarly, Figure 2c,d show the luminance during the middle and end of the total solar eclipse on the totality belt. In Figure 2a, $R_a(S_a c_a)$ and $r_b(M_b c_b)$ are the radii, and c_a and c_b illustrate the centers of the Sun and Moon, respectively, as viewed from the central line of the eclipse shadow. This configuration illustrates the

distance between their centers as observed from any shadow region of the Earth is $D(c_a c_b)$. d_i is the shadow region's width along the centers' joining line. The angle subtended by the point of intersection of the two perimeters and the centers of the Sun and the Moon is α and β . For further computation of obscuration and luminance, we applied the calculation suggested by [32].

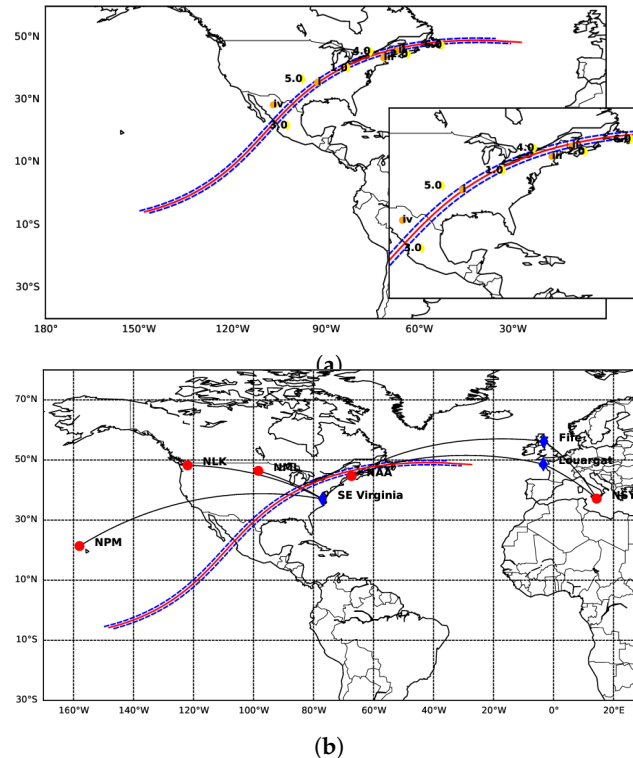


Figure 1. (a) The map illustrates the locations of the GNSS-IGS (yellow diamond) and UNAVCO-IGS (orange circle) stations with the totality belt of the solar eclipse. The red curve depicts the central track of totality. The upper and lower bounds of the total eclipse, represented by the blue dashed curves, indicate the regions where a total eclipse was observed. Outside these dashed curves, only a partial eclipse was visible. (b) Similar map with VLF transmitters with four VLF transmitters (red circles), three receiving locations (blue diamonds) and the great circle path between them.

To analyze the influence of the solar eclipse on the ionosphere, we utilized data from NASA's eclipse archive. This provides the coordinates of the eclipse path (latitude and longitude) as a function of time, defining the central line of the eclipse and its movement across Earth. Based on this path, we calculated the level of obscuration for various locations throughout the eclipse.

We compare the $VTEC$ and in situ N_e data from the Swarm-B satellite on the eclipse day (8 April 2024) to a reference day within the same month to identify changes in the ionosphere caused by the eclipse. The reference day is selected to be a non-eclipse day that Swarm-B satellite passed over the geographic longitude (109.89° W to 110.38° W) between 8° N and 36° N at the same time (08:51–09:03 UT) as on the eclipse day. Only 5 April 2024, met this criterion. On the reference day, Swarm-B satellite was above a region ranging from 119.26° W to 56.11° W from 09:43 to 09:55 UT. The data were accessed from <https://vires.services> on 15 April 2024. Using a combination of computations, we analyze the ionosphere's response to the eclipse through $VTEC$ and N_e data.

We further investigated N_e variations during the eclipse using COSMIC-2 data. We compare the N_e profiles on the eclipse day (8 April 2024) over the totality belt with a reference day (7 April 2024). To ensure a valid comparison, we selected COSMIC-2 data, where the satellite passed over a similar geographic location and at nearly the same time

on both days. These data were accessed from the COSMIC-2 website <https://www.cosmic.ucar.edu/what-we-do/cosmic-2/data> on 11 April 2024.

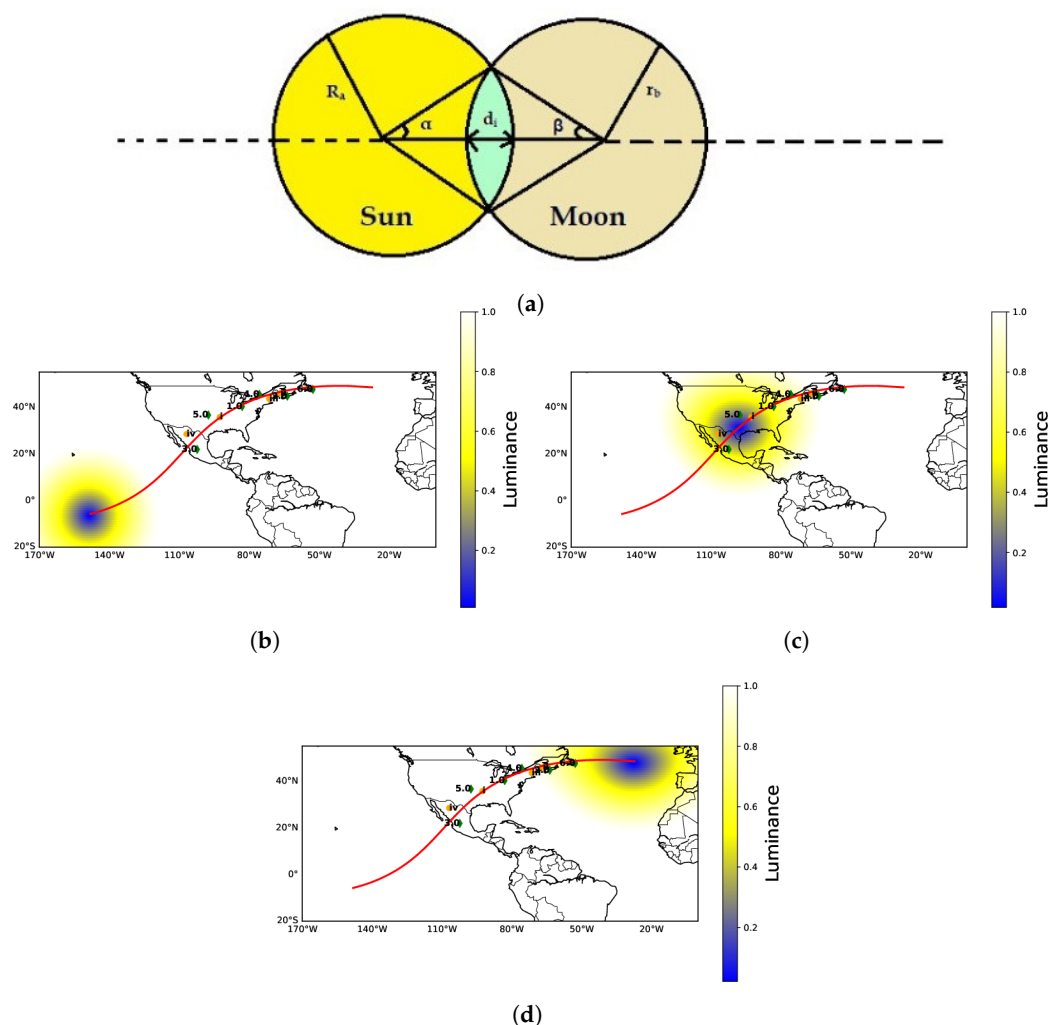


Figure 2. (a) Geometric representation of the Sun and the Moon during a solar eclipse [32]. (b–d) The luminance and lunar shadow at (a) start, (b) mid and (c) end of the eclipse over the totality belt. The colorbar represents the different luminance value over the course of the eclipse.

We present nine *VTEC* maps of ionospheric *VTEC* profiles along the path of totality using GIM data. For the extraction of *VTEC* from the GIM database, we downloaded the data for the eclipse day (8 April 2024) and the non-eclipse days (7 April 2024, and 9 April 2024) from 15:00 UTC to 20:00 UTC. Specifically, we focused on GIM data before the eclipse, during the maximum, and after the eclipse. The data were accessed from the website <https://cddis.nasa.gov> on 12 April 2024. A custom program was developed to analyze the collected raw data, enabling further observations and comparisons between the eclipse and non-eclipse periods. This approach allowed for a detailed examination of how the solar eclipse influences ionospheric *VTEC*, providing insights into electron density dynamics during this celestial event.

The *VTEC* data for producing the DLR's maps were sourced from the website <https://impc.dlr.de/SWE>. The downloaded JSON file was then converted into a format suitable for further analysis. The resultant file was processed using code to plot the maps. To compare the variation of *VTEC* during the solar eclipse, we chose data from three consecutive days: the pre-eclipse day (7 April 2024), the eclipse day (8 April 2024), and the post-eclipse day (9 April 2024). These maps provide a comprehensive

visualization of the *VTEC* distribution and its variations along the path of totality during the eclipse period.

During the solar eclipse, we observed variations in the amplitude of the VLF signal at a receiver located in rural SE Virginia, USA, with coordinates 36.99° N 76.95° W and an elevation of 30 m. The eclipse event at the receiver’s location evolved as follows: first contact occurred at 18:02:53 UT, the maximum eclipse intensity peaked at 19:19:19 UT with a magnitude of 0.834, and last contact was recorded at 20:31:48 UT. During this period, the center of totality was approximately 600 km NW of the receiver.

3. Results

The total solar eclipse was visible from Dallas, and its path spanned from Mexico’s Pacific coast to Newfoundland’s Atlantic coast, covering a narrow strip of the North American continent. While this path experienced totality, a partial solar eclipse was visible across North America, Central America, and Europe. We selected six GNSS-IGS stations from these regions to study the temporal variation of *VTEC* during the eclipse (see Table 1). One station observed the total eclipse, while the other five observed partial eclipses. As shown in Table 1, all stations exhibited a depletion in the *VTEC* during the eclipse. Notably, station HLFX experienced the most significant reduction at 63.56%, while station INEG showed the least reduction at 18.09%. Station NRC1, which encountered 100% obscuration, recorded a *VTEC* depletion of 50.92%. Four stations experienced the eclipse during the forenoon hours, one at noon and one before noon. To illustrate the ionospheric response to the solar eclipse, we present three days of comparative *VTEC* profiles, including the mean of the non-eclipse days (7 and 9 April 2024) and the eclipse day (8 April 2024).

Table 1. List of GNSS-IGS stations.

Station Code	Region	Lat./Long.	Maximum Obsc.(%)	Max Depletion in TEC (%)
(I) NRC1	Canada	45.45° N/ 75.62° W	100	50.92
(II) ACSO	US	40.23° N/ 82.98° W	99.87	40.31
(III) STJO	Canada	47.59° N/ 52.68° W	99.24	52.95
(IV) HLFX	Canada	44.68° N/ 63.61° W	94.29	63.56
(V) SGPO	US	36.60° N/ 97.48° W	93.64	26.06
(VI) INEG	Mexico	21.85° N/ 102.28° W	90.67	18.09

We also investigated the variations in the *VTEC* profiles across different UNAVCO-IGS stations. Data were collected from four stations (see Table 2), with one station experiencing a total solar eclipse while the others observe partial solar eclipses. As shown in Table 2, all stations recorded a depletion in *VTEC* profile. Station P777, experiencing 100% obscuration, showed a 25.95% decrement in *VTEC* profile during the solar eclipse. Stations SA56, P776, and TNCU, which observed partial solar eclipses with obscuration levels of 98.52%, 92.59%, and 90.94%, respectively, also experienced depletion in the *VTEC* profile, with decreases of 54.84%, 59.36%, and 22.37%, respectively.

Table 2. List of UNAVCO-IGS stations.

Station Code (Sl. No.)	Region	Lat./Long.	Maximum Obsc. (%)	Max Depletion in TEC (%)
(I) P777	USA	35.70° N/92.54° W	100	25.25
(II) SA56	Canada	45.95° N/66.64° W	98.52	54.84
(III) P776	USA	43.54° N/71.37° W	92.59	59.36
(IV) TNCU	Mexico	28.45° N/106.79° W	90.94	22.37

We explored the ionospheric response to the solar eclipse by analyzing the diurnal variation of the *VTEC* profile for each station as mentioned above. We accomplished this by using three days of profiles: the eclipse day (8 April 2024; DOY 99) and the two adjacent non-eclipse days (the days with Day of the Year—DOY—numbers 98 and 100, i.e., 7 April 2024, and 9 April 2024, respectively) from which a mean non-eclipse profile is calculated. Figures 3 and 4, which follow the same format, illustrate the variation and percentage change in *VTEC* across three rows for each station, for the GNSS-IGS and the UNAVCO-IGS stations, respectively. Specifically, the first row shows the *VTEC* profile for three consecutive days, color-coded as follows: black for the pre-eclipse day (7 April 2024; DOY 98), red for the eclipse day (8 April 2024; DOY 99), and green for the post-eclipse day (9 April 2024; DOY 100). The middle row displays the mean *VTEC* profile for the two non-eclipse days (black dashed curve) alongside the eclipse day profile (red solid curve). The last row depicts the variation in obscuration as a function of time at all stations (blue solid curve).

During the solar eclipse, we also observe changes in the electron density (*Ne*) profile. Utilizing data from Swarm-B satellite, collected during the same time frame and latitude–longitude as the *VTEC* profile data, Figure 5a illustrates the *Ne* variation during the solar eclipse compared to a reference non-eclipse day. In the top row, the *Ne* profiles for the eclipse day (red curve) and the non-eclipse day (black curve) are depicted across different latitudes with a fixed longitude. The second row displays the difference in *Ne* profiles between the eclipse day and the selected quiet day. Correspondingly, the third row presents the percentage difference in *Ne* profiles. Notably, the *Ne* value decreases by 38% during the eclipse day. Additionally, Figure 5b provides the spatiotemporal variation of *Ne* along with the trajectory of Swarm-B. In this figure, the first vertical line represents the satellite’s track on the reference day, while the second vertical line shows its track on the eclipse day. The red curve over the satellite’s tracks denotes the totality belt. From the color bar, it is clear that the electron density in the intersecting region is higher on the reference day than on the eclipse day. Therefore, we conclude that the electron density during occultation decreases on the eclipse day.

Figure 5c presents a comparative analysis of the *VTEC* profile observed by the Swarm-B satellite during the eclipse and non-eclipse days with an orbital altitude of ~510 km. The top row illustrates the variation of Swarm to GNSS altitude *VTEC* profiles on the eclipse day (red) and the non-eclipse day (black) across different latitudes within a fixed longitude range. The middle panel highlights the difference in *VTEC* values (in TECU) between a reference day and the eclipse day. The third column depicts the percentage change in the *VTEC* profile between the eclipse and non-eclipse days, revealing a maximum *VTEC* depletion of approximately 22%. Additionally, Figure 5d presents the spatiotemporal variation of *VTEC* alongside the track of Swarm-B in the same region during the same time frame. In this figure, the first vertical line represents the satellite’s track on the reference day, while the second line shows its track on the eclipse day. The red curve superimposed on the satellite tracks delineates the path of totality. A comparative analysis of the color bar reveals a pronounced *VTEC* enhancement within the intersecting region during the reference day relative to the eclipse day.

Similarly, Figure 6 presents a comprehensive analysis of the *Ne* profile during both eclipse and non-eclipse days, leveraging data from the COSMIC-2 satellite constellation. The top panel of Figure 6a visually shows the variation of *Ne* profiles on eclipse (depicted in red) and non-eclipse days (depicted in black) across various latitudes and longitude ranges. The middle panel highlights the discrepancy in *Ne* values (measured in electrons per cubic meter) between the reference day and the eclipse day. Notably, the third column illustrates the percentage change in the *Ne* profile between the eclipse and non-eclipse days,

revealing a maximum Ne depletion of approximately 66%. Furthermore, the spatiotemporal dynamics of Ne are illustrated, accompanied by the trajectory of the COSMIC-2 satellite during almost the same time interval. This visualization demonstrates a significant Ne depletion on the eclipse day relative to the reference day profile.

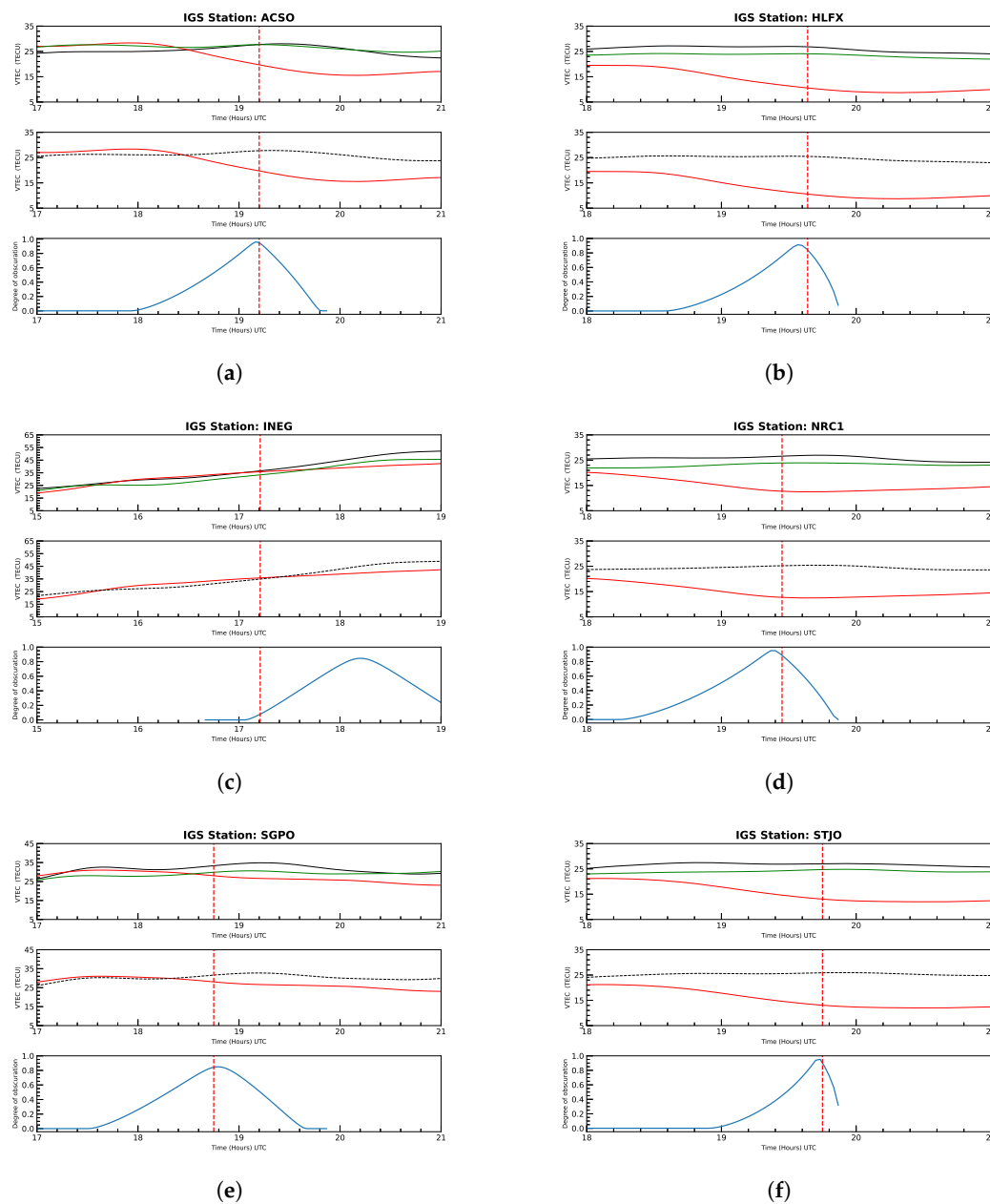


Figure 3. Temporal variation in the $VTEC$ profile as a function of time (UTC) in hours during the solar eclipse as observed from different GNSS-IGS stations as (a) ACSO, (b) HLFX, (c) INEG, (d) NRC1, (e) SGPO and (f) STJO. The upper panel of each profile illustrates the $VTEC$ variation for three consecutive days: the day before the eclipse (black curve), the day of the eclipse (red curve), and the day after the eclipse (green curve). The middle panel shows the mean $VTEC$ variations of the two non-eclipse days (black dashed curve) compared to the eclipse day (red curve). The lower panel indicates the degree of obscuration on the eclipse day.

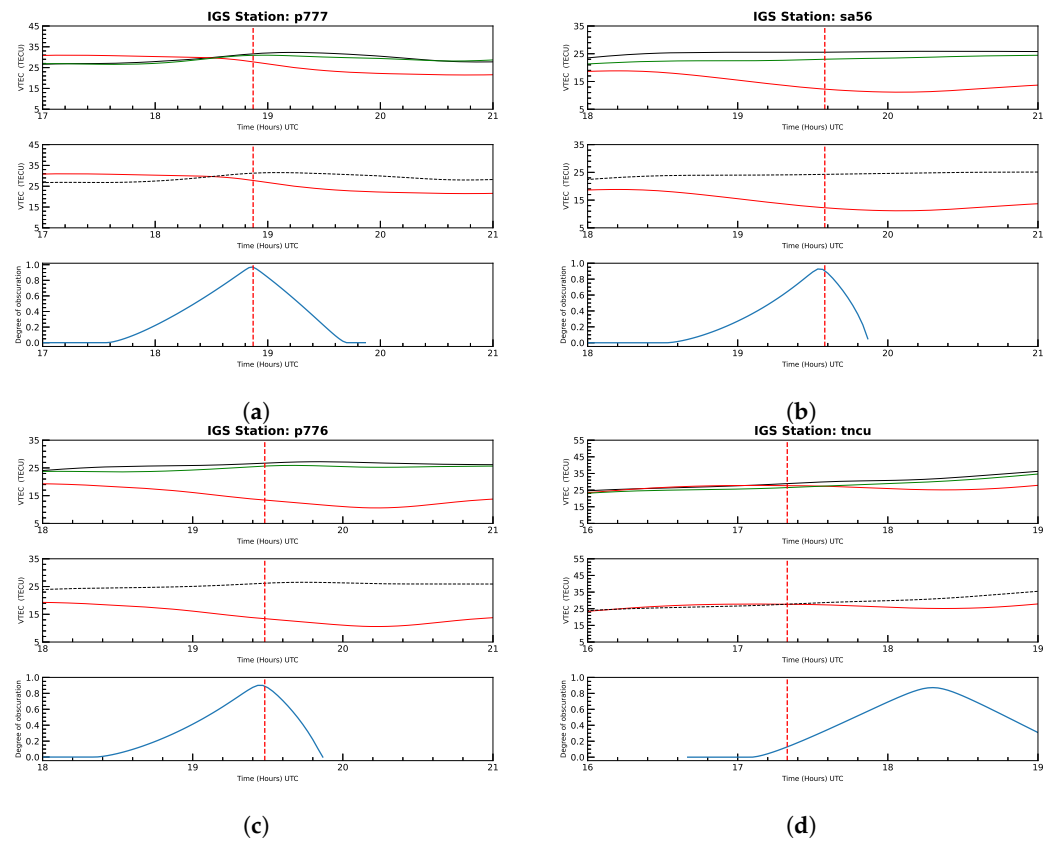


Figure 4. Temporal variation of the $VTEC$ profile as a function of time (UTC) in hours during the solar eclipse for the four UNAVCO-IGS stations: (a) p777, (b) sa56, (c) p776 and (d) tncu. The figure format and color codes are consistent with those in Figure 3.

The Swarm satellite data in the results only cover the partial eclipse phase, not the total eclipse. The depletion noted during this phase shows the effects of the partial eclipse, which may differ from those during the total eclipse. The Swarm satellite data during the total solar eclipse do not show any prominent changes because the data were collected before the eclipse started in the respective region. This nature implies that the signal did not capture the impact of the eclipse. While data are available for 7 and 9 April, they do not meet the criteria relevant to the objective of this study. These dates do not align with the eclipse events that we are investigating, and thus, the data from these days do not contribute to the analysis.

Figure 7 showcases nine maps of ionospheric $VTEC$ profiles along the eclipse path. For comparison, the first and third columns display $VTEC$ variations on non-eclipse days (7 and 9 April 2024). The second column showcases $VTEC$ variations on the eclipse day (8 April 2024) throughout the path, categorized by pre-eclipse, eclipse, and post-eclipse phases. Notably, a significant depletion in the $VTEC$ profile is evident on eclipse days compared to non-eclipse days.

Similar to the GIM data, Figure 8 presents nine ionospheric DLR $VTEC$ maps. These maps depict $VTEC$ variations along the eclipse path. The first and third columns represent the $VTEC$ profiles for the day before the eclipse (April 7, 2024) and the day after the eclipse (9 April 2024), respectively, providing a reference for comparison. The second column showcases the $VTEC$ variations specifically on the eclipse day (8 April 2024). Here, the $VTEC$ variations are further categorized into pre-eclipse, mid-eclipse and post-eclipse time periods to illustrate the changes throughout the totality belt.

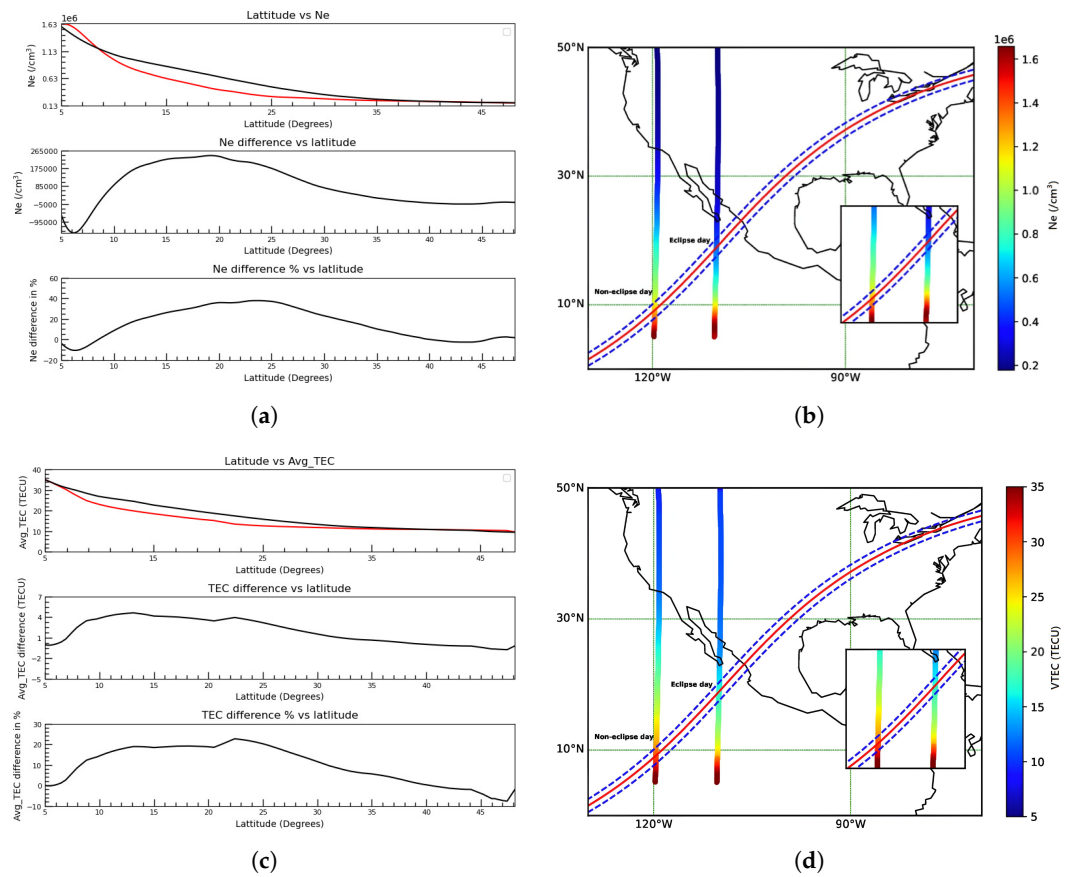


Figure 5. (a) The temporal variation of N_e profiles as a function of latitude as observed from the Swarm satellite. The upper panel shows the N_e profiles for the eclipse day (red curve) and the non-eclipse day (black curve). The middle panel illustrates the difference in N_e profiles between the eclipse day and the non-eclipse day. The lower panel presents the percentage difference in N_e profiles. (b) The spatiotemporal variation of N_e along the trajectory of the Swarm-B satellite. (c) The temporal variation in the average $VTEC$ as a function of latitude as observed from the Swarm satellite. The figure format and color codes are the same as in Figure 5a. (d) The spatiotemporal profile is shown over the satellite track of the Swarm satellite for the eclipse and non-eclipse days.

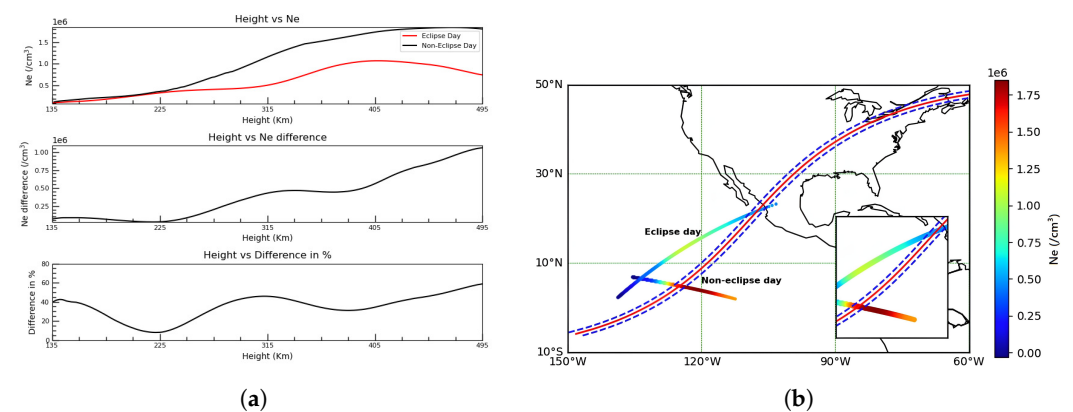


Figure 6. (a) N_e profiles during eclipse and non-eclipse days observed from the COSMIC-2 satellite constellation. The upper panel of each profile illustrates the variation of N_e across a range of latitudes and longitudes, depicting data for eclipse (red curve) and non-eclipse days (black curve). The middle panel displays the difference in N_e values between non-eclipse and eclipse days. The lower panel depicts the percentage change in the N_e profile between eclipse and non-eclipse days. (b) The spatiotemporal profile is shown over the Cosmic satellite track for the eclipse and non-eclipse days.

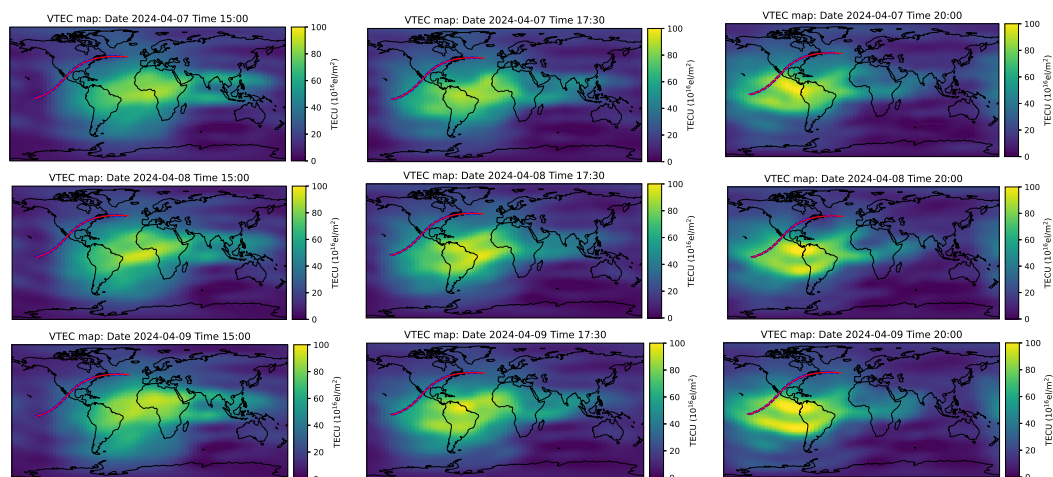


Figure 7. Spatiotemporal profile of VTEC from 15:00 to 20:00 UTC as observed from GIM data for April 7 (top), 8 (middle), and 9 (bottom), 2024.

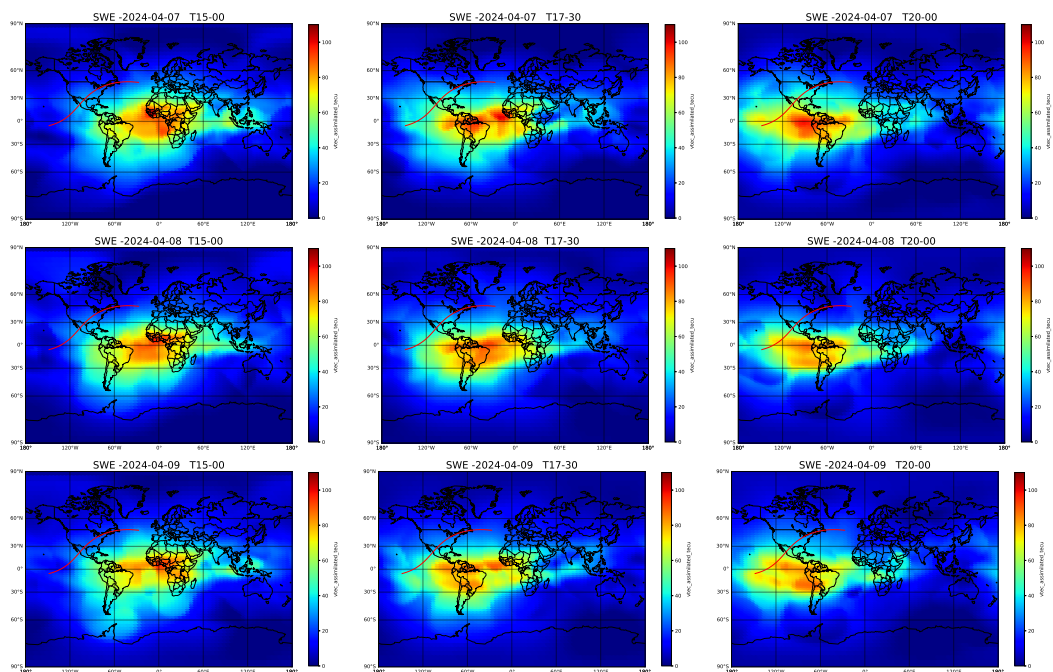


Figure 8. Spatiotemporal profile of VTEC from 15:00 to 20:00 UTC as observed from SWE data for April 7 (top), 8 (middle), and 9 (bottom), 2024.

Figure 9 illustrates a thorough analysis of the VLF amplitude profiles during eclipse and non-eclipse days. In each panel (corresponding to different paths), the top row presents the amplitude profiles for the eclipse day (red curve) and a non-eclipse day (black curve). The second row exhibits the difference in amplitude profiles between the eclipse day and the non-eclipse day. Correspondingly, the third row presents the degree of obscuration with respect to time. For this analysis, we utilized the data of four sub-ionospheric propagation paths and, precisely, the data received at a single receiver located in rural SE Virginia, USA, from four VLF transmitters: NPM, NML, NLK, and NAA. Among these stations, we note a positive amplitude change for three stations and a negative change for NAA. The maximum positive amplitude change recorded is 0.6 dB for NPM. The maximum negative amplitude change observed is 5.25 dB for NAA.

The VLF signal is transmitted from the NAA and NSY transmitters to a receiver located in Fife, Scotland, UK (Figures 10a,b). This received signal corresponds to a unique situation where there was no eclipse at the receiver location, but the VLF signal path from

the transmitter to the receiver experienced the eclipse. Consequently, the eclipse's effect was observed on the VLF signal amplitude. The eclipse time was between 19:30 and 20:00 UTC for both NAA (a) and NSY (b). The positive amplitude change was recorded for both cases, with 7.05 dB for the NAA-Fife path and 7.57 dB for the NSY-Fife path.

We also recorded the VLF signal amplitude at Louargat, France, transmitted from the NAA and NSY transmitters (Figures 10c,d). In this case, the receiver location did not experience any eclipse, but the effect on the VLF amplitude was observed due to the VLF propagation path experiencing the eclipse. The eclipse time was between 19:30 and 20:31 UTC for both NAA (c) and NSY (d). Since we do not have the full-day data for non-eclipse days in this case, we cannot determine the amplitude change between eclipse and non-eclipse days for the NAA-Louargat and NSY-Louargat paths.

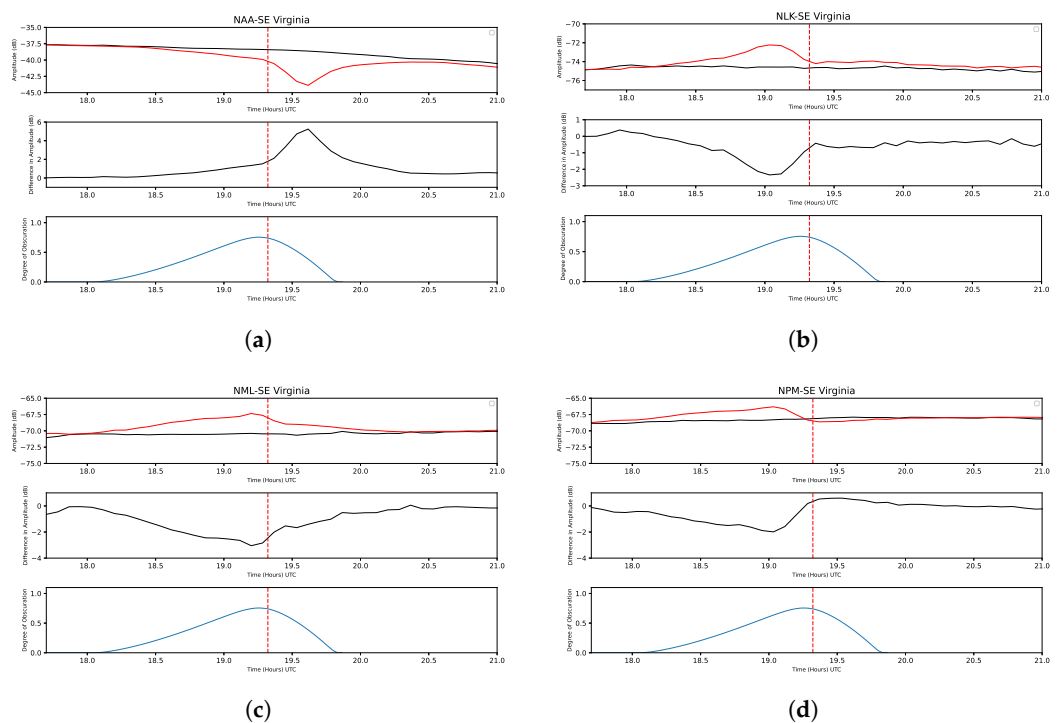


Figure 9. Temporal variation in amplitude profiles during both eclipse and non-eclipse days observed from a VLF receiver located in rural SE Virginia, USA, for the transmitters (a) NAA, (b) NLK, (c) NML and (d) NPM, plotted as a function of time (UTC) in hours. The upper row of each panel compares the amplitude variations for the eclipse day (red curve) and a non-eclipse day (black curve). The middle row illustrates the amplitude profile difference between the eclipse and non-eclipse days. The lower row indicates the degree of obscuration over time.

In Figure 11a,b, the corresponding phase change is presented for the transmitters NPM and NAA. The negative phase change is 63.5° for NPM, and the positive phase change observed is 283.5° for NAA. It is noted that the phase data for the stations NML and NLK are not appropriate for the analysis (corrupted), so these are not presented.

Geomagnetic storms caused by solar activity are known to disrupt the ionosphere. We examined solar and geomagnetic data from 5 April to 11 April 2024 to assess if such a storm influenced the ionosphere during the eclipse. We obtained hourly measurements of Dst (storm intensity), Kp (planetary geomagnetic activity), Ap (auroral electrojet activity), solar flux (F10.7), Lyman-alpha radiation, and the northward component of the interplanetary magnetic field (IMF Bz) from the NASA OMNIWeb database (<https://omniweb.gsfc.nasa.gov/>, accessed on 15 April 2024). Figure 12 shows the observed temporal variations in these parameters (Dst, Kp, Ap etc.) indicating minimal solar and geomagnetic activity around the eclipse period (5 April to 11 April 2024). This observation confirms that our measurements

are not significantly affected by external disturbances, allowing us to attribute the observed ionospheric changes primarily to the solar eclipse.

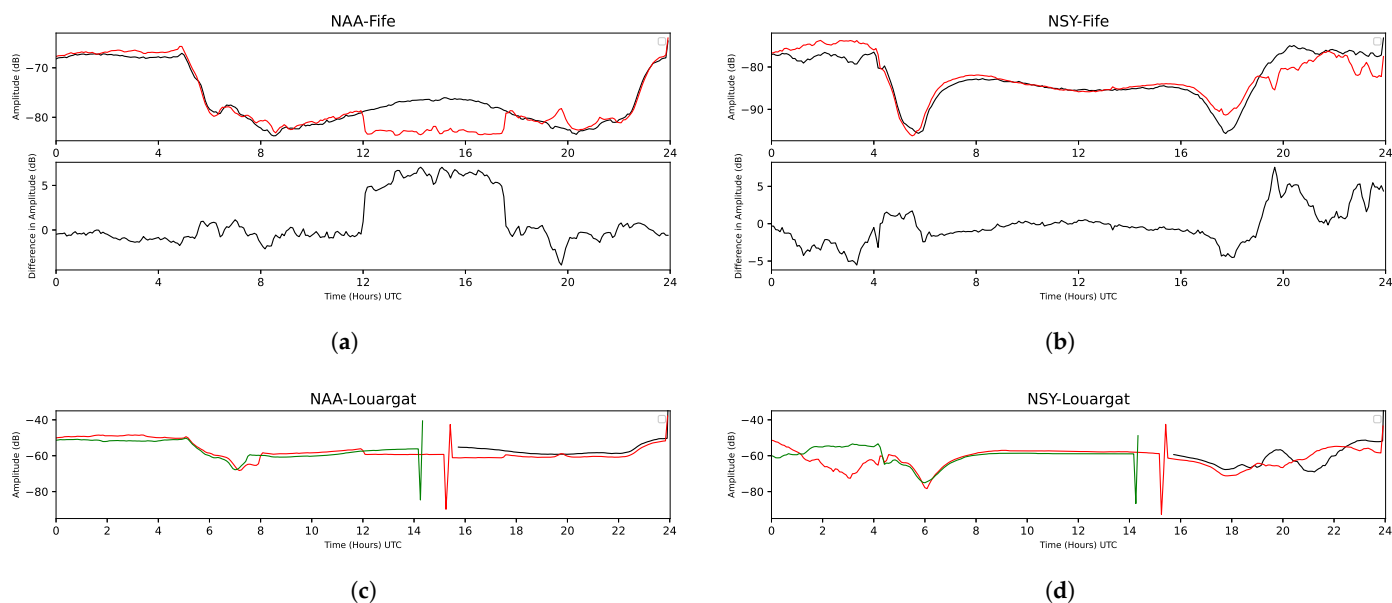


Figure 10. VLF signal amplitude profiles during the eclipse and non-eclipse days observed from a VLF receiver located in Fife, Scotland, for the transmitter–receiver path (a) NAA-Fife and (b) NSY-Fife, plotted as a function of time (UTC) in hours. The upper row of each panel compares amplitude variations for the eclipse day (red curve) and a non-eclipse day (black curve), while the middle row illustrates the amplitude profile difference between the eclipse and non-eclipse days. Similarly, the temporal variation in amplitude profiles during both eclipse and non-eclipse days observed from a VLF receiver located in Louargat, France, for the transmitter–receiver path (c) NAA-Louargat and (d) NSY-Louargat, is plotted as a function of time (UTC) in hours. The red curve represents the eclipse day, and the black and green curves represent non-eclipse days.

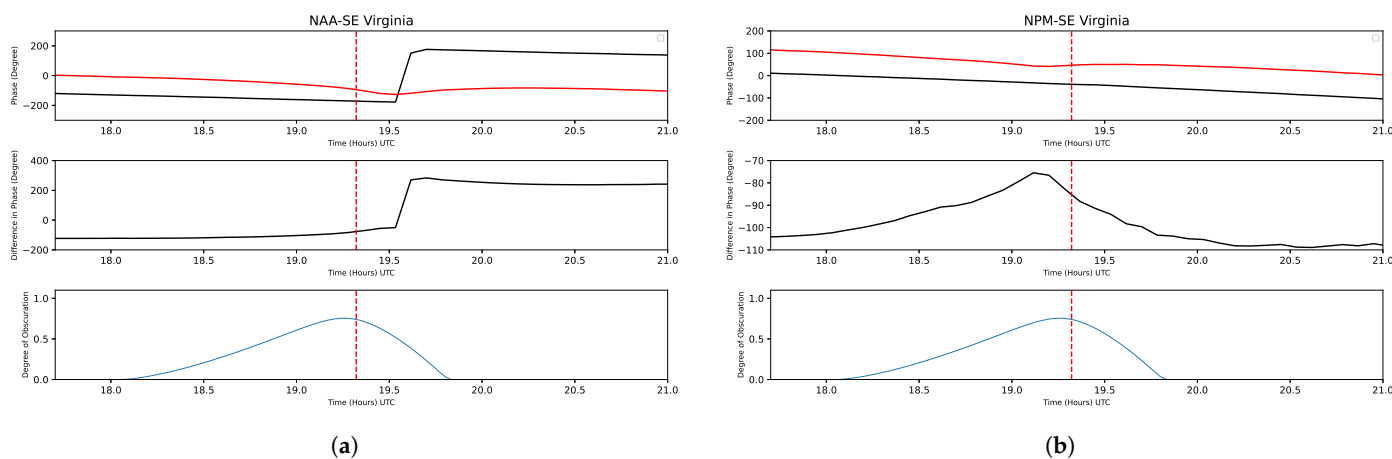


Figure 11. Temporal variation in phase profiles during both eclipse and non-eclipse days as a function of time (UTC) in hours as observed from a VLF receiver located in rural SE Virginia, USA, for the transmitters (a) NAA, (b) NPM. The figure format and color codes per panel are the same as in Figure 9.

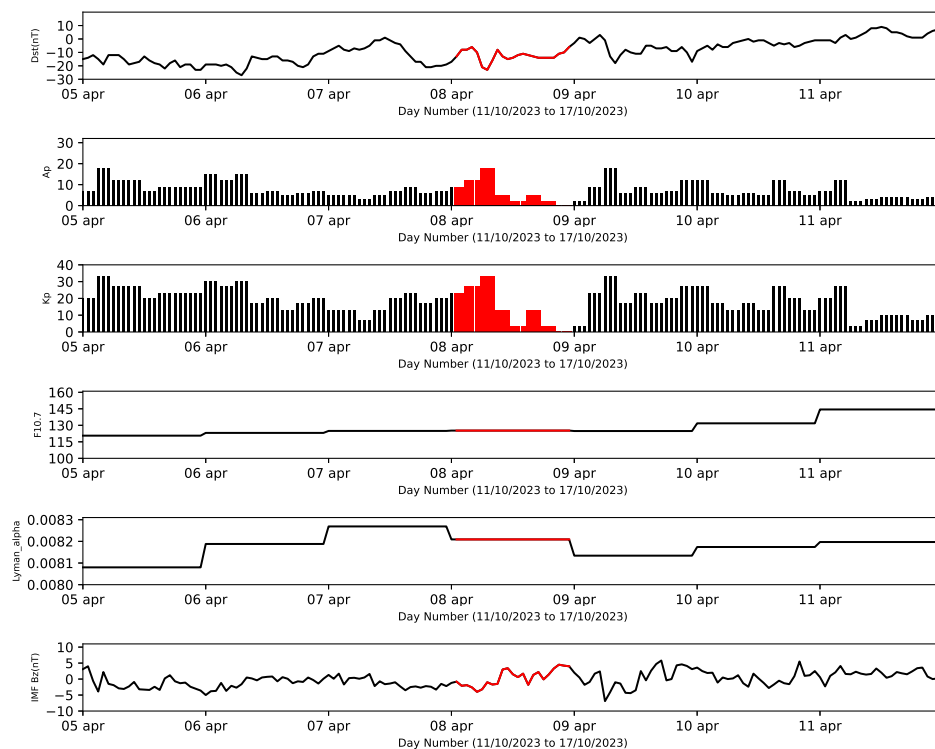


Figure 12. Temporal variation of Dst, Ap, Kp, Solar Flux (F10.7), Lyman alpha, and IMF Bz for the time period 5–11 April, 2024. The red parts of the curves and histograms depict the variation specifically for the eclipse day.

4. Discussion

The manuscript examines the ionospheric response to the total solar eclipse on 8 April 2024, using both ground and space-based observations. The study is conducted under quiet geomagnetic conditions to ensure that our results can be interpreted with a focus on the solar eclipse impact. The modulation in the ionospheric Vertical Total Electron Content (VTEC) is analyzed to attribute ionospheric perturbations to the solar eclipse. The path of the eclipse (see Figure 1) spans a latitude range from 50° N to 10° S and a longitude range from 30° W to 150° E. Data from ten IGS stations, three VLF receiving stations, the GIM database, the DLR's database, the Swarm satellite, and the COSMIC satellite are used to compute both quiet and perturbed VTEC and N_e profiles. The IGS and VLF stations are selected to experience the maximum solar eclipse under varying solar illumination and ionospheric conditions. For instance, some GNSS-IGS stations (NRC1, ACSO, STJO, and HLFX) experience solar radiation blockage in the local afternoon, while SGPO experiences it at noon and INEG in the pre-noon period. Consequently, the VTEC profiles show varied perturbations as illustrated in Figure 3. Similarly, among the UNAVCO-IGS stations, P776 and SA56 experience solar occultation in the local afternoon, P777 at noon, and TNCU in the pre-noon period. The VTEC variations exhibit a combined effect of regular solar flux changes and additional radiation blockage. Solar flux exhibits spatial and temporal variability across different geographic locations. Thus, changes in VTEC can be lower even with higher obscuration and vice versa. The pre-noon and post-noon effects of the eclipse are visible in the TEC profiles. Despite this variability, all stations consistently show a decrease in VTEC during the solar eclipse. VTEC profiles are modeled using data from the GIM and DLR's databases to differentiate between quiet and eclipse-perturbed conditions. Our analysis reveals a depletion in VTEC proportional to the degree of solar obscuration observed VTEC and N_e from Swarm and N_e from COSMIC-2 satellites. This phenomenon

arises from variations in chemical composition coupled with day-to-day fluctuations and differing production and recombination rates across altitudes.

In fact, we used four *VTEC* methods, which, as clarified now in the paper, have different altitude scopes (IGS-DLR GIMs and individual GNSS stations *VTEC* from ground to GNSS altitude, Swarm *VTEC* from Swarm LEO altitude, to GNSS altitude). The *VTEC* changes observed across different data sources, including IGS stations, GIM, DLR, and the Swarm satellite, correlate well. Stations closer to the path of totality consistently showed the data with higher *VTEC* depletion, aligning with the global trends captured by the GIM and DLR databases. Similarly, Ne data from Swarm and COSMIC-2 confirmed the depletion, highlighting the consistency and robustness of the observed ionospheric response to the solar eclipse across different datasets and methodologies. The details are as follows:

1. **IGS Stations:** IGS stations were strategically placed along the eclipse path across North and Central America. Examples include NRC1 (Canada), with 100% obscuration and 50.92% *VTEC* depletion; HLFX (Canada), with 94.29% obscuration and 63.56% *VTEC* depletion; and INEG (Mexico), with 90.67% obscuration and 18.09% *VTEC* depletion. Stations closer to totality exhibited higher *VTEC* depletion, with variations influenced by local geographic and ionospheric conditions.
2. **GIM Database:** The GIM database provided global *VTEC* coverage along the eclipse path, including regions without GNSS stations. It captured spatiotemporal variations before, during, and after the eclipse. The GIM data showed smoother, averaged trends in *VTEC* depletion, revealing global-scale ionospheric effects with significant *VTEC* decreases along the totality belt.
3. **DLR Database:** High-resolution maps (2.5° latitude by 5° longitude) offered detailed views of *VTEC* changes along the eclipse path, focusing on North and South America under total or near-total eclipse. Regional *VTEC* depletion correlated well with the path of totality, providing high-resolution insights into ionospheric responses to varying degrees of obscuration.
4. **Swarm Satellites:** Swarm *Ne* and *VTEC* data were collected along satellite tracks intersecting the eclipse path during partial and total eclipse phases. Latitude-resolved depletion patterns were observed, with a maximum depletion of 22%. While spatial coverage was limited compared to ground-based methods, the data provided valuable vertical profiling of electron density.

The Swarm and COSMIC-2 satellite *Ne* observations of the solar eclipse on April 8, 2024, revealed significant differences in electron density changes based on their respective measurements. The Swarm data indicated a 22% change in electron density as a function of latitude, reflecting the latitudinal impact of the eclipse on ionospheric conditions. In contrast, COSMIC-2 reported a more pronounced 66% change in electron density as a function of altitude, highlighting the vertical ionospheric variations during the eclipse. These complementary observations underscore the complex spatial impact of solar eclipses on the Earth's ionosphere.

During the initial eclipse period, the *VTEC* changes consistently reflected the progression of the solar eclipse. At IGS stations, *VTEC* decreased as the eclipse advanced toward mid-noon, correlating with increasing obscuration. The GIM database captured a global *VTEC* decline, with more pronounced changes near regions experiencing higher obscuration. DLR data highlighted early depletion gradients as the eclipse shadow moved toward totality. Swarm satellite *Ne* data showed initial altitude-specific electron density changes pre-noon, indicating early ionospheric responses, while COSMIC-2 satellites revealed reductions in vertical electron density profiles, marking the onset of ionospheric changes. During the peak eclipse phase, all datasets consistently showed significant *VTEC* depletion, especially near or under totality. IGS stations like HLFX recorded 63.56% deple-

tion with 94.29% obscuration. The GIM database revealed sharp *VTEC* reductions along the path of totality, with smoother trends outward. DLR maps captured peak depletion with distinct latitudinal and longitudinal variations in the totality zone. Swarm satellite data highlighted significant electron density drops at higher altitudes, while COSMIC-2 vertical *Ne* profiles showed maximum depletion of ~66%, at F region altitudes. Post-eclipse, all datasets demonstrated a gradual recovery in *VTEC* and *Ne* as obscuration levels decreased. IGS stations like HLFX and NRC1 showed slow recovery trends, while stations farther from totality recovered more quickly. The GIM database captured a global return to pre-eclipse *VTEC* levels, while DLR maps highlighted regional recovery variations based on prior obscuration and ionospheric conditions. Swarm satellite data showed altitude-specific recovery, particularly at lower latitudes, and COSMIC-2 profiles reflected gradual stabilization of vertical electron density across all altitudes.

The analysis of VLF signal amplitude profiles reveals significant variations during the solar eclipse, highlighting the effects of the eclipse on sub-ionospheric propagation paths. For paths received in rural SE Virginia, USA, positive amplitude changes were observed for NPM, NML, and NLK transmitters, with the maximum recorded at 0.5986 dB for NPM. In comparison, a negative change of 5.25 dB was noted for NAA. Unique effects were observed for VLF signals received in Fife, Scotland, where the receiver did not experience the eclipse. Still, the propagation paths from NAA and NSY did, leading to positive amplitude changes of 7.05 dB and 7.57 dB, respectively. Similarly, for signals received in Louargat, France, the receiver remained outside the eclipse path, yet propagation effects were evident due to the eclipse-affected paths. However, these paths' lack of full-day non-eclipse data prevents a direct comparison. These observations underscore the complex interplay between the VLF propagation characteristics and eclipse-induced ionospheric changes, varying by geographic location and path-specific factors.

The propagation path dependency of VLF signal variations during a solar eclipse highlights the critical role of the geometry and physical characteristics of the Earth-ionosphere waveguide. The behavior of VLF signals is intricately linked to the specific segments of the ionosphere they traverse, as changes in electron density and collision frequency along the propagation path directly influence signal reflection, absorption, and interference patterns. The reduced ionization in the D-region significantly modifies the waveguide's reflective properties for paths that intersect the eclipse region. The lower electron density and decreased collision rates enhance reflection efficiency, allowing signals to propagate with reduced attenuation. This often results in positive amplitude changes, particularly when the geometry of the waveguide supports constructive interference. In contrast, paths that experience phase disruptions due to spatially uneven ionospheric changes can exhibit destructive interference, leading to negative amplitude variations. This is particularly evident in cases like the NAA path, where the -5.25 dB amplitude change may result from disturbances in phase coherence caused by the eclipse-induced ionospheric irregularities. Moreover, the transmitter-receiver distance influences how these variations manifest, as longer paths are more sensitive to cumulative effects of waveguide irregularities and phase shifts. For receivers outside the eclipse path, the dependency on propagation paths becomes even more pronounced. The signal's interaction with the waveguide's eclipsed region dictates amplitude variations in such scenarios. Stations like those in Fife, Scotland, observed significant positive amplitude changes (e.g., 7.05 dB and 7.57 dB for NAA and NSY signals), which can be attributed to the enhanced reflection efficiency in the affected waveguide segment. These variations also depend on the orientation and curvature of the propagation path relative to the eclipse geometry, with longer and more oblique paths exhibiting more complex responses. Additionally, the propagation path dependency is influenced by localized ionospheric conditions, such as the background electron density,

geomagnetic field effects, and time-dependent changes in solar zenith angle. These factors interact dynamically with the eclipse-induced ionospheric perturbations, leading to heterogeneous responses across different paths. This sensitivity underscores the importance of considering the ionosphere's physical properties and the propagation path's geometric alignment to fully understand and predict VLF signal behavior during solar eclipses.

This study stands out by focusing on the variation in the upper atmosphere during a total solar eclipse, leveraging a comprehensive range of space-based and ground-based data worldwide. While many scientists conducted similar research, they typically utilized a more limited set of tools. For instance, using data from six GNSS-IGS stations, [33] examined the *VTEC* profile changes during two different solar eclipses. Similarly, [3] investigated the *VTEC* profile variations during an annular eclipse with data from fifty-five GNSS-IGS stations and the Swarm Satellite, noting that most stations observed a decrease in the *VTEC* profile during solar occultation. Notably, the *VTEC* profile from Swarm shows an almost 28% reduction on the eclipse day compared to the reference day. Our results corroborate previous research demonstrating a decrease in *VTEC* during solar eclipses [34–37].

Recently, [38] presented a multi-instrumental analysis of the same eclipse event, focusing on GNSS-*VTEC*, F-region irregularities using ionosonde measurements, and outcomes from Swarm satellite data. Their results for *VTEC* showed satisfactory agreement with our current study, corroborating many aspects of our findings. However, distinct differences between their data and outcomes are evident. In this manuscript, *VTEC* data from multiple sources, including IGS, UNAVCO, GIM, and DLR maps, were analyzed to examine the depletion profiles. Our results reveal a similar depletion range of 15 to 5 TECU units, consistent with the findings reported by [38]. However, a few stations in our study, notably TNCE and INEG, did not exhibit significant changes. Furthermore, all ten IGS and UNAVCO stations in our analysis were selected from within the 90% lunar obscuration zone, differing from their methodology. To investigate the spatiotemporal profile, we utilized direct data from the GIM and SWE databases to extract changes in *VTEC*. Notably, differences were observed in the electron density profiles derived from Swarm data, likely due to variations in the observation times. While our analysis focused on the interval between 08:51 UT and 09:03 UT, ref. [38] reported their observations between 17:00 UT and 18:20 UT. Additionally, this manuscript extends the scope to include F-layer irregularities and examines the effects on the D-layer through sub-ionospheric VLF wave propagation. Despite employing different approaches, a comparative assessment shows that our results align well with those of [38], providing a complementary perspective on the studied eclipse event.

5. Conclusions

This study leverages the total solar eclipse of 8 April 2024 as a natural experiment to investigate the ionospheric response, focusing on the F-layer dynamics. The changes in Vertical Total Electron Content (*VTEC*) during a solar eclipse are primarily caused by the temporary reduction in solar radiation reaching the Earth's atmosphere. The reduction in solar radiation causes a reduction in the production rate of electrons in the ionosphere. The reduction in temperature and the resulting changes in pressure gradients also influence the atmospheric dynamics, such as the generation of atmospheric gravity waves, which further modulate the ionospheric electron density. These combined effects produce a distinct depletion of *VTEC*, which varies based on the duration, path, and magnitude of the eclipse, as well as the local time and geographic location. By employing a comprehensive multi-instrument approach, which integrates data from ground-based GNSS and VLF stations, space-based observations from Swarm and COSMIC-2 satellites, and spatiotemporal analyses using the Global Ionospheric Map (GIM) and DLR databases, we provide robust

evidence of ionospheric variability during the eclipse. The results consistently reveal a significant depletion in the Total Electron Content (TEC) during the partial and total phases of the eclipse, correlating strongly with the degree of solar obscuration. This reduction in ionization is consistent with the established principle that a decreased solar radiation leads to diminished ionospheric electron densities. Additionally, the VLF signal analysis shows fluctuations in amplitude and phase, complementing the GNSS-based TEC observations and highlighting the eclipse's impact on ionospheric conductivity and wave propagation. Geomagnetic data confirm that external space weather disturbances do not influence the results, validating the isolation of eclipse-induced effects. This study's findings enhance our understanding of ionospheric dynamics during solar eclipses and underscore the utility of multi-instrument campaigns for capturing spatiotemporal variability in the ionosphere.

The reduction in electron density (Ne) observed during the solar eclipse is consistent with established ionospheric physics. Electron density in the ionosphere results from a dynamic equilibrium between ionization, driven by solar extreme ultraviolet (EUV) and X-ray radiation and recombination processes. During the eclipse, the Moon's shadow significantly attenuates EUV and X-ray flux, leading to a sharp decrease in ion production rates and, consequently, Ne . In the absence of sufficient ionizing radiation, recombination processes dominate. These processes, particularly effective in the lower ionospheric regions with higher neutral densities, further accelerate the reduction in Ne . Spatial variations in the eclipse-induced Ne changes are attributed to factors such as local solar zenith angle, geomagnetic field inclination, and atmospheric composition, which influence the ionization and recombination rates. Altitude-dependent effects are also significant, with the slower recombination rates in the F-region contributing to delayed recovery compared to the E-region. The observed reduction aligns with the theoretical predictions, attributing transient decreases in Ne during eclipses to disruptions in the balance between photoionization and recombination. Additionally, the eclipse induces thermospheric cooling due to diminished solar heating, which alters the neutral density and atmospheric composition, indirectly affecting ionospheric chemistry and plasma dynamics. Gravity waves generated by rapid cooling and heating during the eclipse may further influence Ne variations.

This manuscript contributes a comprehensive investigation of the ionospheric response to the total solar eclipse, as it integrates observations of both the lower and upper ionospheres using ground-based and space-based instruments. The study provides a multi-layered perspective on eclipse-induced ionospheric changes by leveraging VLF signal data to capture the lower ionospheric perturbations and satellite-derived $VTEC$ profiles to analyze the upper ionospheric dynamics. This dual approach allows for a detailed characterization of ionospheric processes, including variations in electron density, production and recombination rates, and propagation effects along eclipse-affected paths. Such an integrative methodology offers new insights into the coupling mechanisms between the ionosphere's layers, enriching the understanding of solar-terrestrial interactions during eclipses. Future research will focus on integrating high-resolution models and extending observational networks to explore the coupling between ionospheric and thermospheric responses during eclipses, offering deeper insights into the interplay between solar radiation and upper atmospheric processes.

Author Contributions: Conceptualization, S.S., A.D. and S.M.P.; methodology, S.S. and A.D.; software, A.S., B.B., S.K.M. and S.S.; validation, S.S., B.B., A.D., H.H. and G.B.; formal analysis, A.S., B.B. and S.K.M.; investigation, S.S., A.D., S.K.M., H.H. and G.B.; resources, S.J., J.M.P., P.N., G.S.W. and J.B.; data curation, A.S., B.B., S.K.M., S.M.P., A.K.M. and S.S.; writing—original draft preparation, A.D., S.M.P. and S.S.; writing—review and editing, S.M.P., P.P., A.K.M. and S.R.; visualization, P.P. and S.R.; supervision, A.D. and S.S.; project administration, S.S. All authors have read and agreed to the published version of the manuscript.

Funding: Georgios Balasis' work has been supported as part of Swarm DISC (Data, Innovation, and Science Cluster) activities, funded by ESA contract no. 4000109587.

Informed Consent Statement: Not applicable.

Data Availability Statement: The open-source data are available on their corresponding websites as mentioned in the manuscript.

Acknowledgments: The authors acknowledge Prof. Gopi K. Seemala for providing the GPS-TEC software for the major computation. The authors also acknowledge the IGS, Swarm, COSMIC, GIM, SWE, and NASA Omniweb database team members for various data used in this article.

Conflicts of Interest: The authors declare no conflicts of interest.

Abbreviations

The following abbreviations are used in this manuscript:

VTEC	Vertical Total Electron Content
STEC	Slant Total Electron Content
GIM	Global Ionospheric Map
IGS	International GNSS Service
GNSS	Global Navigational Satellite System
VLF	Very Low Frequency
UNAVCO	University NAVSTAR Consortium

References

1. Kumar, S.; Kumar, A.; Maurya, A.K.; Singh, R. Changes in the D region associated with three recent solar eclipses in the South Pacific region. *J. Geophys. Res. Space Phys.* **2016**, *121*, 5930–5943. <https://doi.org/10.1002/2016JA022695>.
2. Mitra, A.P. Ionospheric effects of solar flares. *Astrophysics and Space Science Library*; D. Reidel Publishing Company, Boston, MA, USA; 1974; Volume 46. <https://doi.org/10.1007/978-94-010-2231-6>
3. Das S.; Maity, S.K.; Nanda, K.; Jana, S.; Brawar, B.; Panchadhyayee, P.; Datta, A.; Sasmal, S. Study of the response of the upper atmosphere during the annular solar eclipse on October 14, 2023. *Adv. Space Res.* **2024**, *74*, 3344–3360. <https://doi.org/10.1016/j.asr.2024.06.021>
4. Maurya, A.K.; Phanikumar, D.V.; Singh, R.; Kumar, S.; Veenadhari, B.; Kwak, Y.-S.; Kumar, A.; Singh, A.K.; Niranjana Kumar, K. Low-mid latitude D region ionospheric perturbations associated with the 22 July 2009 total solar eclipse: Wave-like signatures inferred from VLF observations. *J. Geophys. Res. Space Phys.* **2014**, *119*, 8512–8523. <https://doi.org/10.1002/2013JA019521>.
5. Zhang, R.; Le H.; Li, W.; Ma, H.; Yang, Y.; Huang, H.; Li, Q.; Zhao, X.; Xie, H.; Sun, W.; et al. Multiple technique observations of the ionospheric responses to the 21 June 2020 solar eclipse. *J. Geophys. Res. Space Phys.* **2020**, *125*, e2020JA028450. <https://doi.org/10.1029/2020JA028450>
6. Kundu, S.; Chowdhury, S.; Palit, S.; Mondal, S.K.; Sasmal, S. Variation of ionospheric plasma density during the annular solar eclipse on December 26, 2019. *Astrophys. Space Sci.* **2022**, *367*, 44. <https://doi.org/10.1007/s10509-022-04069-y>
7. Fathy, A.; Ghamry, E.; Arora, K. Mid and low-latitudinal ionospheric field-aligned currents derived from the Swarm satellite constellation and their variations with local time, longitude, and season. *Adv. Space Res.* **2019**, *64*, 1600–1614. <https://doi.org/10.1016/j.asr.2019.07.022>
8. Friis Christensen, E.; Lühr, H.; Hulot, G. Swarm: A constellation to study the Earth's magnetic field. *Earth Planets Space* **2006**, *58*, 351–358. <https://doi.org/10.1186/BF03351933>
9. Friis-Christensen, E.; Lühr, H.; Knudsen, D.; Haagmans, R. Swarm—An Earth observation mission investigating geospace. *Adv. Space Res.* **2008**, *41*, 210–216. <https://doi.org/10.1016/j.asr.2006.10.008>
10. Hussien, F.; Ghamry, E.; Fathy, A.; Mahrous, S. Swarm Satellite Observations of the 21 August 2017 Solar Eclipse. *J. Astron. Space Sci.* **2020**, *37*, 29–34. <https://doi.org/10.5140/JASS.2020.37.1.29>
11. Olsen, N.; Friis-Christensen, E.; Floberghagen, R.; Alken, P.; Beggan, C.D.; Chulliat, A.; Doornbos, E.; Da Encarnação, J.T.; Hamilton, B.; Hulot, G.; et al. The Swarm satellite constellation application and research facility (SCARF) and Swarm data products. *Earth Planets Space* **2013**, *65*, 1189–1200. <https://doi.org/10.5047/eps.2013.07.001>
12. Jakowski, N.; Mayer, C.; Hoque, M.M.; Wilken, V. Total electron content models and their use in ionosphere monitoring. *Radio Sci.* **2011**, *46*, 1–11. <https://doi.org/10.1029/2010RS004620>

13. Bracewell, R.N. Theory of formation of an ionospheric layer below E layer based on eclipse and solar flare effects at 16 kc/sec. *J. Atmos. Terr. Phys.* **1952**, *2*, 226–235. [https://doi.org/10.1016/0021-9169\(52\)90033-0](https://doi.org/10.1016/0021-9169(52)90033-0)
14. Crary, J.H.; Schneible, D.E. Effect of the eclipse of 20 July 1963 on VLF signals propagating over short paths. *J. Res. Natl. Bur. Stand. Sect. Radio Sci.* **1965**, *69D*, 947–957. <https://doi.org/10.6028/jres.069d.103>
15. Sen Gupta, A.; Goel, G.K.; Mathur, B.S. Effect of the 16 February 1980 solar eclipse on VLF propagation. *J. Atmos. Terr. Phys.* **1980**, *42*, 907–909. [https://doi.org/10.1016/0021-9169\(80\)90107-5](https://doi.org/10.1016/0021-9169(80)90107-5)
16. Clilverd, M.A.; Rodger, C.J.; Thomson, N.R.; Lichtenberger, J.; Steinbach, P.; Cannon, P.; Angling, M.J. Total solar eclipse effects on VLF signals: Observations and modeling. *Radio Sci.* **2001**, *36*, 773–788. <https://doi.org/10.1029/2000RS002395>
17. Chakrabarti, S.K.; Sasmal, S.; Chakraborty, S.; Basak, T.; Tucker, R.L. Effects of ionospheric disturbances on very low frequency signals. *Adv. Space Res.* **2018**, *62*, 651–661. <https://doi.org/10.1016/j.asr.2018.05.006>
18. Chakrabarti, S.K.; Pal, S.; Sasmal, S.; Mondal, S.K.; Ray, S.; Basak, T.; Maji, S.K.; Khadka, B.; Bhowmick, D.; Chowdhury, A.K. Ionospheric anomalies associated with solar eclipses studied using VLF signals. *J. Atmos.-Sol.-Terr. Phys.* **2012**, *86*, 65–70. <https://doi.org/10.1016/j.jastp.2012.06.006>
19. Pal, S.; Chakrabarti, S.K.; Mondal, S.K. Modeling of sub-ionospheric VLF signal perturbations associated with total solar eclipse, 2009 in Indian subcontinent. *Adv. Space Res.* **2012**, *50*, 196–204. <https://doi.org/10.1016/j.asr.2012.04.007>
20. Cheng, W.; Xu, W.; Gu, X.; Wang, S.; Wang, Q.; Ni, B.; Lu, Z.; Xiao, B.; Meng, X. A comparative study of VLF transmitter signal measurements and simulations during two solar eclipse events. *Remote Sens.* **2023**, *15*, 3025. <https://doi.org/10.3390/rs15123025>
21. Ercha, A.; Zhang, S.R.; Erickson, P.J.; Goncharenko, L.P.; Coster, A.J.; Jonah, O.F.; Lei, J.; Huang, F.; Dang, T.; Lei, L. Coordinated ground-based and space-borne observations of ionospheric response to the annular solar eclipse on 26 December 2019. *J. Geophys. Res. Space Phys.* **2020**, *125*, e2020JA028296. <https://doi.org/10.1029/2020JA028296>
22. Reeve, C.D.; Rycroft, M.J. The eclipsed lower ionosphere as investigated by natural very low frequency radio signals. *J. Atmos. Terr. Phys.* **1972**, *34*, 667–672. [https://doi.org/10.1016/0021-9169\(72\)90154-7](https://doi.org/10.1016/0021-9169(72)90154-7)
23. Klobuchar, J.A. Design and characteristics of the GPS ionospheric time delay algorithm for single frequency users. *IEEE Trans. Aerosp. Electron. Syst.* **1987**, *AES-23*, 325–331. <https://doi.org/10.1109/TAES.1987.310829>
24. Seemala, G.; Valladares, C. Statistics of total electron content depletions observed over the South American continent for the year 2008. *Radio Sci.* **2011**, *46*, 1–14. <https://doi.org/10.1029/2011RS004722>
25. Kundu, S.; Sasmal, S.; Chakrabarti, S.K. Long-term ionospheric VTEC variation during solar cycle 24 as observed from Indian IGS GPS station. *Int. J. Sci. Res. Phys. Appl. Sci.* **2021**, *94*, 1–12. <https://doi.org/10.26438/ijrpsas/v9i4.112>
26. Bagiya, M.; Joshi, H.; Iyer, K.; Aggarwal, M.; Ravindran, S.; Pathan, B.M. TEC variations during low solar activity period (2005–2007) near the Equatorial Ionospheric Anomaly Crest region in India. *Ann. Geophys.* **2009**, *27*, 1047–1057. <https://doi.org/10.5194/angeo-27-1047-2009>
27. Marković, M. Determination of total electron content in the ionosphere using GPS technology. *Geonauka* **2014**, *2*, 1–9. <https://doi.org/10.14438/gn.2014.22>
28. Rama Rao, P.V.S.; Niranjan, K.; Prasad, D.S.V.V.D.; Gopi, Krishna, S.; Uma, G. On the validity of the ionospheric pierce point (IPP) altitude of 350 km in the Indian equatorial and low-latitude sector. *Ann. Geophys.* **2006**, *24*, 2159–2168. <https://doi.org/10.5194/angeo-24-2159-2006>
29. Rama Rao, P.V.S.; Gopi, K.S.; Niranjan, K.; Prasad, D.S.V.V.D. Temporal and spatial variations in TEC using simultaneous measurements from the Indian GPS network of receivers during the low solar activity period of 2004–2005. *Ann. Geophys.* **2006**, *24*, 3279–3292. <https://doi.org/10.5194/angeo-24-3279-2006>
30. Rao, P.; Seemala, G.; Niranjan, K.; Prasad, D. Study of spatial and temporal characteristics of L-band scintillations over the Indian low-latitude region and their possible effects on GPS navigation. *Ann. Geophys.* **2006**, *24*, 1567–1580. <https://doi.org/10.5194/angeo-24-1567-2006>
31. Eyelade, V.A.; Adewale, A.O.; Akala, A.O.; Bolaji, O.S.; Rabi, A.B. Studying the variability in the diurnal and seasonal variations in GPS total electron content over Nigeria. *Ann. Geophys.* **2017**, *35*, 701–710. <https://doi.org/10.5194/angeo-35-701-2017>
32. Möllmann, K.P.; Vollmer, M. Measurements and predictions of the illuminance during a solar eclipse. *Eur. J. Phys.* **2006**, *27*, 1299. <https://doi.org/10.1088/0143-0807/27/6/021>
33. Valdés-Abreu, J.C.; Díaz, M.; Bravo, M.; Stable-Sánchez, Y. Ionospheric Total Electron Content Changes during the 15 February 2018 and 30 April 2022 Solar Eclipses over South America and Antarctica. *Remote Sens.* **2023**, *15*, 4810. <https://doi.org/10.3390/rs15194810>
34. Vyas, B.M.; Sunda, S. The solar eclipse and its associated ionospheric TEC variations over Indian stations on January 15, 2010. *Adv. Space Res.* **2011**, *49*, 546–555. <https://doi.org/10.1016/j.asr.2011.11.009>
35. Kumar, S.; Priyadarshi, S.; Gopi Krishna, S.; Singh, A.K. GPS-TEC variations during low solar activity period (2007–2009) at Indian low latitude stations. *Astrophys. Space Sci.* **2012**, *339*, 165–178. <https://doi.org/10.1007/s10509-011-0973-6>
36. Hoque, M.M.; Wenzel, D.; Jakowski, N.; Gerzen, T.; Berdermann, J.; Wilken, V.; Minkwitz, D. Ionospheric response over Europe during the solar eclipse of March 20, 2015. *J. Space Weather. Space Clim.* **2016**, *6*, A36. <https://doi.org/10.1051/swsc/2016032>

37. Senapati, B.; Huba, J.D.; Kundu, B.; Gahalaut, V.K.; Panda, D.; Mondal, S.K.; Catherine, J.K. Change in total electron content during the 26 December 2019 solar eclipse: Constraints from GNSS observations and comparison with SAMI3 model results. *J. Geophys. Res. Space Phys.* **2020**, *125*, e2020JA028230. <https://doi.org/10.1029/2020JA028230>
38. Zhang, H.; Zhang, T.; Zhang, X.; Yuan, Y.; Wang, Y.; Ma, Y. Multi-Instrument Observations of the Ionospheric Response Caused by the 8 April 2024 Total Solar Eclipse. *Remote Sens* **2024**, *16*, 2451. <https://doi.org/10.3390/rs16132451>

Disclaimer/Publisher’s Note: The statements, opinions and data contained in all publications are solely those of the individual author(s) and contributor(s) and not of MDPI and/or the editor(s). MDPI and/or the editor(s) disclaim responsibility for any injury to people or property resulting from any ideas, methods, instructions or products referred to in the content.